IEEE Access
Multidisciplinary | Rapid Review | Open Access Journal

Received February 8, 2018, accepted April 3, 2018, date of publication April 17, 2018, date of current version May 24, 2018.

Digital Object Identifier 10.1109/ACCESS.2018.2825397

A Generative Model for OCT Retinal Layer Segmentation by Groupwise Curve Alignment

WENJUN DUAN[1], YUANJIE ZHENG[2,3,4], YANHUI DING[1], SUJUAN HOU[1], YUFANG TANG[5], YAN XU[5], MAOLING QIN[1], JIANFENG WU[6], DINGGANG SHEN[7,8], AND HONGSHENG BI[9]

[1]School of Information Science and Engineering, Shandong Normal University, Jinan 250014, China
[2]Key Laboratory of Intelligent Computing and Information Security, School of Information Science and Engineering, University of Shandong , Jinan 250100, China
[3]Shandong Provincial Key Laboratory for Distributed Computer Software Novel Technology, Institute of Biomedical Sciences, Shandong Normal University, Jinan 250014, China
[4]Key Laboratory of Intelligent Information Processing, Shandong Normal University, Jinan 250014, China
[5]School of communication, Shandong Normal University, Jinan 250014, China
[6]School of Ophthalmology and Optometry, Shandong University of Traditional Chinese Medicine, Jinan 250355, China
[7]Department of Radiology and Biomedical Research Imaging Center, The University of North Carolina at Chapel Hill, Chapel Hill, NC 27599, USA
[8]Department of Brain and Cognitive Engineering, Korea University, Seoul 02841, South Korea
[9]Eye Institute, Shandong University of Traditional Chinese Medicine, Jinan 250355, China

Corresponding author: Yuanjie Zheng (zhengyuanjie@gmail.com)

This work was supported in part by the Natural Science Foundation of China under Grant 61572300 and Grant 61702313, in part by the Natural Science Foundation of Shandong Province, China, under Grant ZR2014FM001 and Grant ZR2016FQ20, in part by the Taishan Scholar Program of Shandong Province, China, under Grant TSHW201502038, in part by the Primary Research and Development Plan of Shandong Province under Grant 2017GGX10112, in part by the Postdoctoral Science Foundation of China under Grant 2017M612338, and in part by the Shandong Science and Technology Plan Project under Grant J17KB177.

ABSTRACT Retinal layer segmentation from optical coherence tomography (OCT) is of fundamental importance for measuring retinal layer thicknesses. These thickness measurements have been shown to correlate well with the severity of different ocular diseases; hence, they provide useful diagnostic information concerning diseases. Manual segmentation of retinal layers from OCT remains dominant in ophthalmological clinical practice but has serious drawbacks: it is time consuming, labor intensive, and results in inter/intra-rater variations. Computer aided segmentation has attracted intensive research attention because it holds the potential not only to provide repeatable, quantitative, and objective results but also to reduce the time and effort required to delineate the retinal layers. However, most of the existing computer based retinal layer segmentation techniques focus on segmenting specific layers by exploring their unique characteristics; thus, they can fail to segment a retinal layer that is totally different. In this paper, we propose a generative retinal layer segmentation method based on groupwise curve alignment that combines the capabilities of segmenting different retinal layers into a unified framework. This method is unique for both its accuracy and its ability to segment any retinal layer without any special modifications. We experimentally validate that the proposed method outperforms a representative state-of-the-art technique by using images of both normal healthy eyes and diseased eyes. Our method is potentially useful in a large variety of practical applications involving retinal layer segmentation from OCT.

INDEX TERMS Optical coherence tomography (OCT), retinal layer segmentation, dynamic time warping, joint curve matching.

I. INTRODUCTION

Optical coherence tomography (OCT) enables micrometer-resolution retinal imaging—both at the optic nerve head and the macula—and has become an established imaging modality in ophthalmology. Retinal layer segmentation from OCT is of fundamental importance for measuring retinal layer thicknesses, a measurement that correlates well with the severity of different ocular diseases and, hence, provides useful diagnostic information concerning possible diseases. Manual segmentation of retinal layers from OCT remains dominant in ophthalmological clinical practice but has serious drawbacks: it is time consuming, labor intensive and results in inter/intra-rater variations. Computer aided segmentation has attracted intensive research attention because it

holds the potential not only to provide repeatable, quantitative and objective results but also to reduce the time and effort required to delineate the retinal layers.

Until now, published and available computer based retinal layer segmentation techniques fall into two groups, either fully automated or human intervention. With a fully-automated method, computer algorithm determines the specific interfaces with no human supervision. Most of these techniques focus on segmenting desired retinal layers by exploring their unique photometric or geometric characteristics within a layer area or at layer boundaries via intensity-variation measurement [1], pixel classification [2], Markov boundary modeling [3], edge detection [4], texture and shape analysis [5], machine learning techniques [2] image registration [6], and so on. Among these techniques, the graph-theory based segmentation approaches [7] have been successful in various medical image segmentation applications, and they are superior to the classic shortest path algorithms [8]–[13]. However, most of these methods can deteriorate and produce limited accuracy for real retinal images that have low contrast between layers and severe retinal deformities [14]–[16].

Human intervention is required to initiate or refine the segmentation result, which usually requires the experts to place seed points and the computer interpolating the layers via point-fitting algorithms [17]. The interactive methods usually need human to add or delete seed points until the algorithm adequately demarcated the layer [18]. While the gross errors of interface mis-detection frequented in the automated techniques are avoided, the manual methods usually time-consuming and subjective [19], and generally yield higher inter-grader variability. Additionally, without special technical re-design or experimental re-training (for classification-based approaches) most existing computer-based retinal layer segmentation approaches fail to segment totally different retinal layers or even the same retinal layers but from different species (e.g., human vs canine [20]). Such limitations confine the application of the related techniques to a very specific domain.

To overcome the limitations of the existing techniques for segmenting retinal layers from OCT, we propose a generative retinal layer segmentation method based on groupwise curve alignment. This method is unique both for its accuracy in retinal layer segmentation and for its ability to segment any retinal layer without any special modifications. Specifically, we treat the profile formed by the OCT image intensities along each A-scan as a curve and align the curves from the different A-scans in a groupwise manner. The spatial correspondences between the curves obtained from the groupwise curve alignment process offer information that can determine a retinal layer boundary when any boundary point is manually specified. The proposed model first applies pairwise curve matching to establish initial maps between the curves points. Additionally, in order to ensure the accuracy of the synthesis results, we applies a groupwise matching process that solves a constrained optimization problem [21], [22] by taking advantage of all the pairwise maps to generate a set of optimized maps.

The main contributions of this paper are as follows.

(1) We present an early work on semi-automated segmentation of retinal layers from OCT that can delineate the boundaries of any retinal layer after a single boundary point is manually specified.
(2) We propose an alternative strategy for retinal layer segmentation from OCT that involves a groupwise curve alignment. This strategy avoids the drawbacks of the current most popular method for examining the special characteristics of retinal layer's area/boundary.
(3) We propose a powerful segmentation tool derived from the groupwise curve alignment that provides an opportunity to correct the errors in pairwise maps using a constrained combinatorial optimization process.
(4) Our framework of multilayer segmentation can segment any stratified structure appearing in the OCT image without any special technical re-design or experimental re-training.

The remainder of this paper is organized as follows: Section 2 discusses existing works related to curve alignment. Section 3 provides a detailed description of the proposed model. Section 4 presents our experimental results and discussions, and Section 5 concludes this paper and gives directions for future work.

II. RELATED WORK

A. CLASSICAL WORKS ON DTW

Dynamic time warping (DTW) [23] is an essential point-to-point matching algorithm, which provides a solution to the global optimal alignment path (as illustrated in Figure 1). DTW has been widely adopted in a variety of applications such as speech processing [24], human motion alignment [25] and time series classifications [26]–[28].

At present, several variants of DTW exist that were designed sequentially. For example, derivative dynamic time warping (dDTW) [29] takes the first-order derivatives of sequences into account when calculating the distance matrix, and then selects the intuitively correct feature for feature alignment by DTW between two time series. Weighted DTW [30] differs from dDTW; it is a penalty based DTW that utilizes the phase difference between two points to compute a similarity matrix. Theoretically, these approaches improve the accuracy of the results and achieve computational efficiency in different ways, but their measurements of the similarity between two points depends solely on their single-point y-values.

Some other algorithms have been proposed to find the warping more efficiently based on various constraints. Most of these algorithms do not compute the full accumulative distance matrix between two sequences. For instance, [31] employs compulsive band constraints on the potential warping path to increase the computational efficiency of dynamic

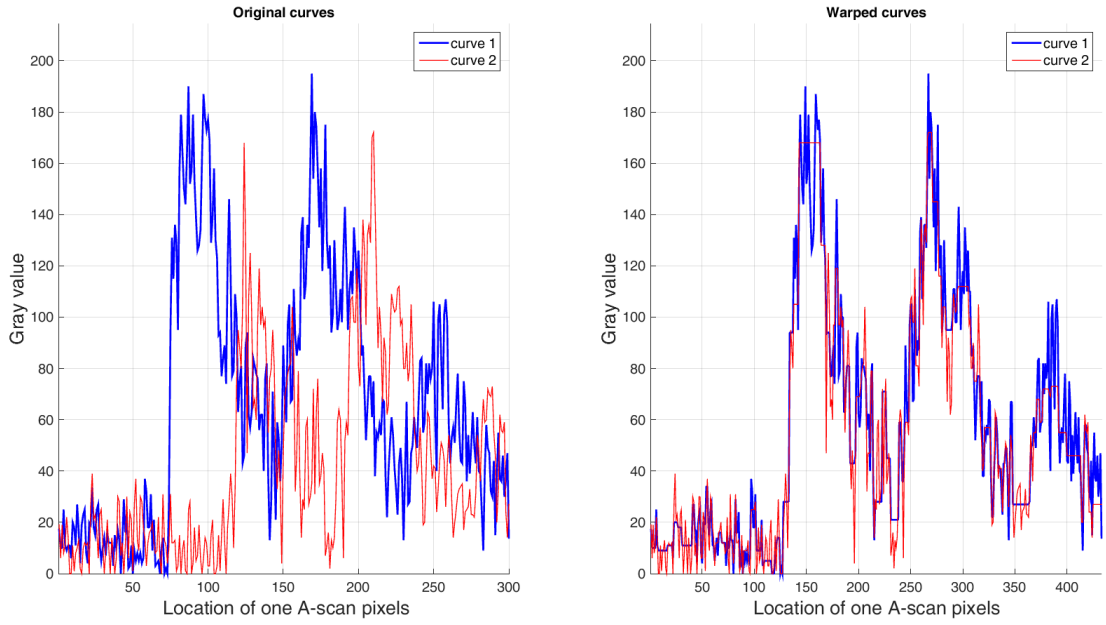

FIGURE 1. Example of pairwise A-line alignment by DTW. From left to right: the original gray curves from two different A-lines; the blue and red colors indicate DTW-aligned local structures.

time warping. Similarly, [24] introduces global warping path constraints to improve the efficiency and prevent pathological warping. The authors utilize series local structure information to constrain the search of the warping path. In detail, they first respectively detect and match feature points using a SIFT feature point detector and descriptor; then, they regularize the scope of the warping path according to the matched point pairs.

The algorithm used in our model, shapeDTW [32], is different from the above studies in that the pairwise point distances are encoded by the similarities between their local neighborhoods. Specifically, the major objective of this study is to improve the accuracy of the results by employing descriptors to express the spatial position and structure information of each point. Based on these ideas, shapeDTW was developed to align series sequences that may be locally deformed by stretching, shifting and contractions, but for which better alignments can be achieved. In our case, gray-scale waveforms of every A-scan from one OCT retinal image are determined by the structural information of biological tissues. Concretely, two sets of points from their corresponding A-scans that have extremely similar structures can be matched by shapeDTW under a condition in which the thicknesses of the identical tissues from different locations are likely to exhibit inhomogeneity.

B. EXISTING RESEARCH ON JOINT MATCHING

In the last few years, joint object matching has become an emerging topic that utilizes the cycle-consistency criterion to prune outliers. This algorithm has also become a fundamental algorithm in computer vision because it has numerous applications such as finding correspondences across a set of images [21], determining non-rigid structures from motion [33], [34], and solving jigsaw puzzles [35]. Moreover, joint matching can also find consistent relations from given pairwise matches, which are often very noisy and contain many false and missing matches [36].

Many off-the-shelf joint matching algorithms [37], [38] aim at obtaining consistent shape maps from a large collection of similar relations. These consistency based approaches usually comprise two steps. First, a pairwise object-matching method is devised to estimate the computed correspondence between overall pairs of objects. Then, a spectrum smoothing technique [39] is employed to maximize the pairwise feature affinities and cycle consistency across multiple images. Specifically, Pachauri *et al.* [37] focused on the "permutation synchronization" problem, which employs spectral techniques via eigenvector decomposition to create the initial all-pairwise matching solutions and generates a set of optimized maps. But the program assumes that the matching matrices over all object pairs are corrupted by Gaussian-Wigner noise. Chen *et al.* [40] aggregated information from a collection of objects with partial similarities to improve the densely corrupted correspondences between map pairs. This method relies on the assumption that the underlying rank of the variable matrix can be reliably estimated [21], and it solves the tractable convex programming problem using a metabolic first-order Alternating Direction Method of Multipliers (ADMM). More recently, the problem has been formulated as one of finding the closest positive semidefinite matrix to an input matrix that stores the overall pairwise maps [22], [36]. This family of methods is based on the observation that the constraint of cycle-consistency can be mapped to the low-rank and positive semidefinite matrices

of an initial input matrix. However, the computational efficiency of the semidefinite approach limits its use in real applications [21].

In contrast to the previously described methods, we employ a global optimization-based approach [21] to identify true or false pairwise matches by checking all the cycles in the curve collection. This method formulates the problem as a low-rank recovery problem that can spontaneously fulfill the desired semidefiniteness of a solution and, simultaneously, derive a fast alternating minimization algorithm to optimize thousands of points. Our experimental results show that this method has extremely good performance, and it has good results in optimizing the curve alignments of each A-scan from one OCT retinal image.

III. PROPOSED APPROACH

This section introduces our generalized method for segmenting the layered structures of retina from OCT volumes. Here, we assume that each scan of OCT retinal volumes has n A-scans, each of which contains m pixels, and that a correspondence exists between the points in any pair of curves for all A-scans. For each scan, the framework of our generative semi-automatic segmentation strategy is as follows:

(1) First, each pixel is represented by a slope descriptor. Specifically, each original real-valued sequence $f_\alpha = [x_1, x_2, x_3, \ldots, x_m]^T$, $\alpha \in \{1, n\}$, is converted to a sequence of slope descriptors, denoted as $D_\alpha = [d_1, d_2, d_3, \ldots, d_m]^T$, $D \in R^{m\times s}$.

(2) Second, the transformed multivariate descriptor sequences, D, are aligned by DTW. Finally, the alignment path between the descriptor sequences is transferred to the original A-scan intensity sequences to form binary correspondence matrices $(L_{i,j})_{\alpha,\beta}$. Then, the pairwise matches between the points of all curves are encoded by a large binary matrix $L \in \{0, 1\}^{nm\times nm}$.

(3) Third, we apply the global optimization-based approach to improve the pairwise correspondence results L by pruning false matches and outputting the results with higher correspondences $X \in \{0, 1\}^{nm\times nm}$.

(4) Finally, the spatial correspondences between the pairwise curves obtained from the curve alignment process offer information for determining the retinal layer boundary when any single boundary point is manually specified.

A. DESCRIPTOR

The intensity inhomogeneity in the OCT image often leads to a y-shift. Concretely, the same tissue in different positions may have exactly the same shape in the A-scan series, but a y-shift exists between them. Therefore, we use the multidimensional slope descriptor to represent the subsequences. Then, we provide the implementation details of the subsequence descriptor computation at each point.

Let the intensity from an A-scan be denoted by f_α, and the gray level sequence be obtained from individual A-scans. We build a subsequence p_i constituted by the nearest l points from x_i. Next, we divide the subsequence p_i into s equal-square overlapping or non-overlapping intervals; the dimension of each interval should be smaller than the length of the subsequence l. In our task, referring to the results of recent work, we empirically set $l = 20$ and $s = 4$. With respect to each interval, we adopt the total least square (TLS) line fitting algorithm [41] to fit a line based on the points that fall within each interval. Finally, we obtain an s-dimensional vector descriptor by incorporating the slopes of the fitted lines from all the intervals to describe the point x_i, i.e., $d_i = f_{slope}(p_i)$ [32].

B. DYNAMIC TIME WARPING

For each possible input curve combination (α, β), dynamic time warping can introduce a pairwise matching matrix $L_{\alpha\beta} \in \mathbf{R^{m\times m}}$ that recovers the optimal alignments between two sets of points from their corresponding A-scan series.

Here, we single out a sample to reveal the computational process of dynamic time warping. The alignment of two descriptor subsequences $D_\alpha = [d_1, d_2, \ldots, d_m] \in \mathbf{R^{s\times m}}$ and $D_\beta = [t_1, t_2, \ldots, t_m] \in \mathbf{R^{s\times m}}$ is optimal in the sense that it minimizes a cumulative distance measure consisting of local distances [42]. To make the simulations generic, we construct a sum-of-squares cost function:

$$J_{dtw}(P) = \min \sum_{r=1}^{k} \|d_{p_r^x} - t_{p_r^y}\|^2. \tag{1}$$

In Eq. (1), P is a correspondence matrix that stores a pair of path vectors $P = \left[p^\alpha, p^\beta\right]^T \in \mathbf{R^{2\times k}}$, where p^α and p^β represent the corresponding indexes of the descriptors in the sequence, respectively. The parameter k represents the number of steps needed to align the descriptor series. Therefore, $P_t = \left[p_t^\alpha, p_t^\beta\right]^T = [i, j]^T$ when the i^{th} descriptor in D_α and the j^{th} descriptor in D_β are aligned.

Then, the goal is to find the path associated with the least cost. The least cost problem can be solved effectively by dynamic programming [43]. To make the optimization tractable, as emphasized in previous work, we construct the following three constraints:

1) Boundary condition: A warping path is a concatenation of nodes starting from node (1, 1) and ending with node (m, m). Specifically, all the warping paths start from the step $P_1 = [1, 1]^T$ and end at the step $P_k = [m, m]^T$.
2) Monotonicity: $p_{r1} - p_{r2} \leq 0$, if $r_1 \leq r_2$.
3) Continuity: $P_r - P_{r-1} \in \{[0, 1]^T, [1, 0]^T, [1, 1]^T\}$.

Finally, the iteration-dependent function is defined as follows:

$$L^*(P_r) = \min_{w(P_r)} \|d_{p_r^\alpha} - t_{p_r^\beta}\|^2 + L^*(P_{r+1}). \tag{2}$$

Eq. (2) can be solved in $(O(m \times m))$ time by Bellman's equation. In this section, the objective cost function $L^*(P_r)$ denotes the remaining cost starting at the r^{th} step to be incurred following the optimum policy w, where

$w : \{1 : m\} \times \{1 : m\} \mapsto \{[0, 1]^T, [1, 0]^T, [1, 1]^T\}$ denotes the allowed transition between consecutive steps, i.e., $p_{t+1} = p_t + w(p_t)$. Fig. 2 shows an alignment path resulting from aligning two series using DTW.

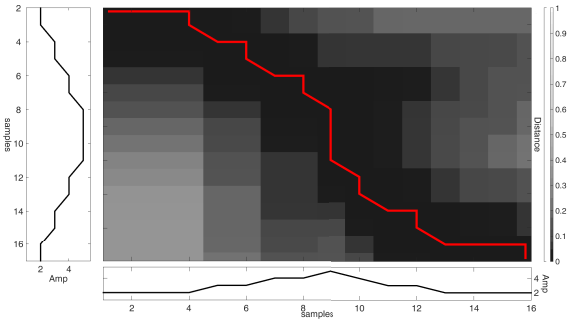

FIGURE 2. An example of two curve alignment paths. Samples: the curves to be matched. Amp: the amplitude of curve.

The pairwise matching binary matrix $L_{\alpha\beta}$ can be constructed by the correspondence matrix P from the starting point. For instance, the (i_{th}, j_{th}) element in this matrix is 1 when $\left[p_t^\alpha, p_t^\beta\right]^T = [i, j]^T$. The process of descriptor alignment leads to a set of $\left(L_{i,j}\right)_{\alpha,\beta}$, which is formulated as a concatenated matrix:

$$\mathbf{L} = \begin{pmatrix} L_{1,1} & L_{1,2} & \dots & L_{1,n} \\ \vdots & \vdots & \ddots & \vdots \\ L_{n,1} & L_{n,2} & \dots & L_{n,n} \end{pmatrix}$$

where $L_{\alpha,\beta} = 1$ if α is equal to β.

C. JOINT CURVE MATCHING

In the following, we describe our constrained optimization formulation in a basic setting, where the input is the correspondences, L, and the output consists of cycle consistent correspondences $X = \{X_{\alpha,\beta} : f_\alpha \mapsto f_\beta, 1 \le \alpha, \beta \le n\}$ between the input curves. The cycle consistency and joint matching via fast alternating minimization are introduced as follows.

1) CYCLE CONSISTENCY

Recently, there has been growing interest in jointly matching many shapes [44]–[46], using the constraint of cycle consistency [22], [37], [40], [47]. Before introducing the proposed method, we first provide a brief introduction to the cycle consistency model, under which the joint matching capability is the easiest to interpret.

Consider a collection of n curves, each containing m points. Moreover, suppose that a correspondence exists between the points in any pair of curves (f_α, f_β). Mathematically, one can consider the ground truth as each point x_d^i in f_α having one or more natural counterparts x_t^j in f_β. We say that the system of correspondences for any three curves (α, β, γ) is consistent if $x_d^i \sim x_t^j$ and $x_t^j \sim x_q^o$ together imply that $x_d^i \sim x_q^o$, where x_q^o in f_γ. Consequently, the cycle consistency can be described by $X_{\alpha,\gamma} = X_{\alpha,\beta}X_{\beta,\gamma}$. This framework can also be extended to cases involving more objects.

The results of the present work [22], [37] reveal that the cycle consistency can be expressed more concisely by giving a virtual reference ordering (named "universe") that is defined as the set of unique descriptors $d_1, d_2, d_3, \dots, d_z$ that appear in the curve descriptor collection. Each element in this ordering is contained in at least one object f_α. The true point mapping between a curve and the universe ordering can be encoded as $A_\alpha \in \{0, 1\}^{m\times z}$, where z is the number of descriptors in the universe ordering. Then, the ground-truth correspondences between the αth and βth curves can be represented by $X_{\alpha,\beta} = A_\alpha A_\beta^T \in \{0, 1\}^{m\times m}$. As map matrices, $X_{\alpha,\beta}$ should satisfy the following double stochastic constraints:

$$0 \le X_{\alpha\beta}1 \le 1, 0 \le X_{\alpha\beta}^T 1 \le 1. \tag{3}$$

We use a block matrix $X \in \{0, 1\}^{N\times N}$ where $N = nm$ to encode the entire collection of partial correspondences $X = \{X_{\alpha,\beta} : f_\alpha \mapsto f_\beta, 1 \le \alpha, \beta \le n\}$. Supposing that all the $A_\alpha s$ are concatenated as rows in a matrix $A \in \{0, 1\}^{N\times z}$, the ground-truth correspondence over all the points can be denoted as follows:

$$\mathbf{X} = \begin{pmatrix} X_{1,1} & X_{1,2} & \dots & X_{1,n} \\ \vdots & \vdots & \ddots & \vdots \\ X_{n,1} & X_{n,2} & \dots & X_{n,n} \end{pmatrix} = AA^T. \tag{4}$$

Following the standard Eq.(4), it is easy to see that a desired X should be both positive semidefinite and low-rank:

$$X \ge 0, \quad rank(X) \le z. \tag{5}$$

As Eq. (5) clearly shows, the consistency can be effectively imposed without checking every cycle of the pairwise matches. Furthermore, due to the bijection hypothesis (i.e., $X_{\alpha,\gamma} = X_{\alpha,\beta}X_{\beta,\gamma}$), partial matching is allowed.

2) JOINT MATCHING VIA RANK MINIMIZATION

The provided pairwise matches over the points in two curves are encoded by $L \in R^{nm\times nm}$, which is a noisy version of AA^T. The joint matching concerns the recovery of the globally consistent matches, X. Instead of using semidefinite programming relaxation, we formulate the problem as a low-rank matrix recovery problem and employ the nuclear-norm relaxation approach for rank minimization.

To make the optimization tractable, we perform the following two modifications to X. (1) We replace the binary matrix X by a real matrix $X \in [0, 1]^{nm\times nm}$. This approach is practical when solving matching problems; it constrains the values of X to the range $[0, 1]$. Both theoretical and experimental results prove that the solution values in X are much closer to 0 or 1. (2) We maintain the rank of X as the sum of singular values. The nuclear norm $||X||_*$ is a tight convex relaxation that has been shown to be extremely effective in multifarious low-rank problems.

Moreover, concerning the doubly sub-stochastic constraints in Eq. (3), we propose three additional constraints:

(1) Self-matching is treated as an identity matrix:

$$X_{\alpha\alpha} = I^{m\times m}, \quad 1 \le \alpha \le n. \tag{6}$$

(2) X must be a symmetric matrix:

$$X_{\alpha\beta} = X^T_{\beta\alpha}, \quad 1 \le \alpha, \beta \le n. \alpha \ne \beta. \tag{7}$$

(3) The values in X are within [0,1]:

$$0 \le X \le 1. \tag{8}$$

To guarantee that the recovery is close to the real map, one alternative measure is to maximize the correspondence agreement between $X_{\alpha\beta}$ and $L_{\alpha\beta}$ for any pair of curves. Inspired by these works, we propose the following formulation: $\sum_{\alpha=1}^{n}\sum_{\beta=1}^{n} < L_{\alpha\beta}, X_{\alpha\beta} >$. Furthermore, to induce the sparsity, we propose an objective function, $\eta < 1, X >$, that minimizes the sum of values in X, where η represents a regularization parameter that balances the agreement to the sparsity structure. Experimentally, we set $\eta = 0.5$ in our task. As mentioned before, the rank of X is replaced by the weighted nuclear norm $\lambda||X||_*$. All three terms lead to our cost function [21]:

$$F(X) = -\sum_{\alpha=1}^{n}\sum_{\beta=1}^{n} < L_{\alpha\beta}, X_{\alpha\beta} > +\eta < 1, X > +\lambda||X||_* \tag{9}$$

where $< ., . >$denotes the inner product. For computational simplicity, the form $\eta 1 - L$ is replaced by Z; consequently, we obtain the following optimization function:

$$\min_X < Z, X > +\lambda||X||_* \quad s.t. X \in \Gamma, \tag{10}$$

where Γ denotes the set of matrices satisfying the constraints of Eqs. (6)–(8).

With regard to the state-of-the-art methods in [25], the result does not degrade noticeably when removing the positive semidefinite constraint and the doubly stochastic constraint. This result might be attributable to the existence of the sparsity regularization $\eta < 1, X >$. The positive semidefinite constraint has been ignored for the following reasons: (1) The constraints of X self-matching are identity and symmetric. (2) The solution to Eq. (10) turns out to be nearly positive semidefinite. (3) When λ is sufficiently large, the negative values of a matrix, if they exist, are negligible compared to the norm of the matrix. Based on our experimental observations and referring to the results of recent work, we set $\lambda = 80$.

Most advanced off-the-shelf methods such as alternating direction methods of multipliers (ADMM) [48] or the proximal method [49] used to solve the nuclear norm minimization in Eq.(10) are typically based on iterative singular value thresholding [50], which must be performed in each iteration. However, this approach is extremely computationally expensive even for medium-sized problems. For practical applications, recent works on low-rank optimization [51] attempt to solve the problem more efficiently via a change of variables $X = AB^T$, where $A, B \in R^{N\times u}$ are new variables with a smaller dimension, $u < N$.

In Eq. (10), $||X||_*$ is defined as below

$$||X||_* = \min_{A,B} \frac{1}{2}(||A||_F^2 + ||B||_F^2), \tag{11}$$

and Eq. (10) becomes

$$\min_{X,A,B} < Z, X > +\frac{\lambda}{2}||A||_F^2 + \frac{\lambda}{2}||B||_F^2 \quad s.t. X = AB^T, X \in \Gamma \tag{12}$$

which can be minimized by ADMM as detailed in [21].

D. DEALING WITH 3D DATA

The above processes of our framework account for a segmentation of retinal layers in 2D image. It can be extended to volumetric segmentation with a series of tricks as demonstrated in Fig.3 and detailed below:

(1) Expert used the computer mouse to place the seed point at a desired OCT layer of first B-scan of the volume, the marked image as a reference image, and coordinate of the point is (x, y) (the point at the top left is $(0, 0)$). We employ the marked B-scan as a reference image.

(2) We first detect the yth column on each B-scan. We then apply the dynamic time warping algorithm described in III to establish maps between each pair of curves successively. Now that we have obtained the points from each of the remaining B-scan corresponding to the seed point.

(3) Then the computer automatically interpolated the layer based on the optimized maps X. The spatial correspondences between the A-scans obtained from the groupwise curve alignment process offer information for determining a retinal layer boundary when a seed point is manually specified. The strategy used for surface from the remaining B-scans were same as those used in the reference image.

(4) In order to make the detected interface smooth, we fit a cubic spline surface based on the points extracted from each A-scan via the group-wise alignment process.

IV. EXPERIMENTS

A. IMAGE DATA

Data from the eyes of 54 subjects were obtained with a Heidelberg Spectralis OCT system, and each volume contained $908 \times 50 \times 408$ voxels centered on the fovea and recorded a $6 \times 6 \times 2\ mm^3$. Of the 54 subjects, 27 were diagnosed with posterior detachment of vitreous, 18 were diagnosed with pigment epithelium uplift and neuroepithelium effusion, while the remaining 9 were health controls. We split the data into two groups, dataset1 contains 9 volumes acquired from the retinas of normal healthy eyes, and dataset2 consists of 45 3-D OCT volumes acquired from the diseased eyes.

The ground truth slices showing the marked layer interfaces were created by two trained ophthalmologists using

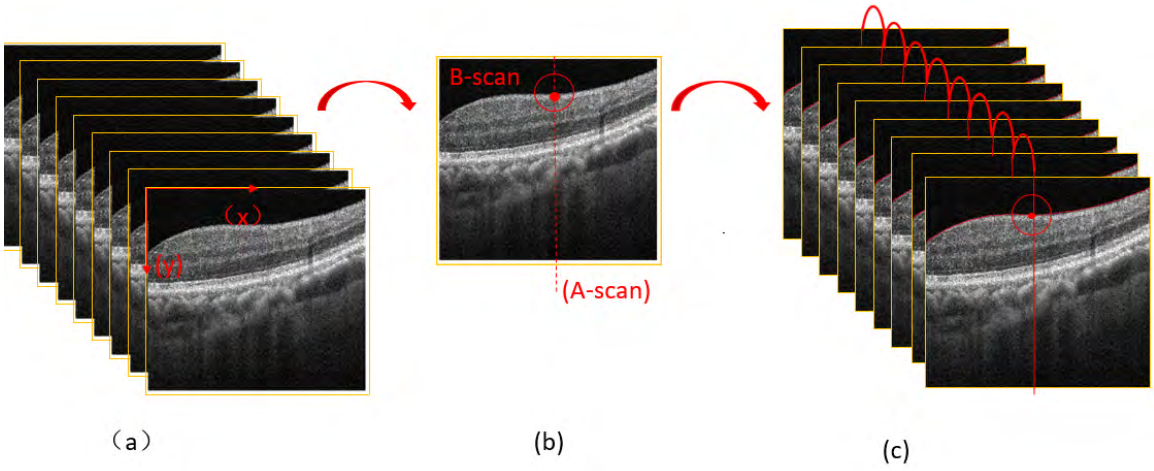

FIGURE 3. (a) Example OCT cube. (b) Example B-scan within the cube, formed by a series of A-scans at each horizontal location. The red point in the red circle is a hand-marked seed point. (c) Seed points of the unmarked slices are obtained by aligning group-wisely the marked A-scan and the corresponding A-scans in unmarked slices.

Adobe Photoshop. All experiments demonstrate that our method is unique for its accuracy not only for retinal layer segmentation but for any layered structure, such as a choroid.

B. IMAGE PREPROCESSING

The OCT retinal layer imaging technique generates a cross-sectional image by recording the axial reflectance profiles while the transverse position of the optical beam on the sample is scanned. Thus, an OCT image is a map of the reflectivity of the sample. The principle of optical imagery leads to the fact that OCT images contain speckle noise and gray-intensity inhomogeneities. Intensity normalization can cause the intensity values observed in a particular tissue type to be approximately the same within an image and across populations of images. Just as in most current OCT retinal layer segmentation algorithms, in our algorithm it is also important that the gray intensity values of the image are consistent. To reduce the effect of speckle noise, many current studies employ a preprocessing strategy such as a median filter [3], [52], mean filter [1], diffusion filter [13], [16], or directional filter [53]. Then, because the edge sharpness is affected by the de-noising procedure, the subsequent segmentation performance is also reduced. In addition, most of the previous algorithms do not consider the intensity inhomogeneity in the OCT imaging process, and this neglect can also lead to inaccurate segmentation and an inability to detect all the layers.

Thus, as a coarse de-noising preprocessing step, an averaging filter with a size of 25 pixels was first applied to each image. Then, to address the intensity inconsistency issues, which is necessary to enhance the contrast between the different layers, we rescaled the contrast of the images by setting the intensity values smaller than P_m to 0, while those pixels with intensity values larger than P_m are set to unity. The threshold P_m was found by calculating the median of the corresponding A-scan and interpreted as a robust maximum of the data. This preprocessing maintains the overall intensity values and edge information while simultaneously removing the hyperintense reflections found at the surface of the retina in the B-scan. An example result of this normalization step is shown in Fig. 4(b).

C. EXPERIMENTAL ENVIRONMENT AND ASSESSMENT

The experiments implemented the proposed algorithm in MATLAB, and the two data sets were processed on a computer with 8 GB of RAM and a CORE i5 CPU @ 3.30 GHz. For comparison, the average positioning of two independent observers were treated as the reference standard in our evaluation. The mean signed and unsigned positioning errors for the ILM, NFL/GCL, IPL/INL, INL/OPL, OPL/ONL, ONL/OLM, ISP, OSP/RPE, RPE/BRC, CHR/SCL and pathological structure boundaries were computed.

This paper developed a generative model to segment OCT images of human retinal layers, and demonstrated the algorithm's excellent performance. We compared our semi-automated results against the reference standard by computing the mean and standard deviation (shortest distance of a point on an algorithm-produced border to a manually-specified border) of the unsigned and signed retinal layer positioning errors. Fig. 5 shows the samples of the intera-retinal boundaries found by the manual and the proposed methods. As a baseline comparison, we also performed the same evaluation using a graph-based multi-surface segmentation method. This approach was similar to the techniques proposed in [11] and has been shown to produce highly accurate segmentations of retinal layers in macular OCT images of patients. Nevertheless, for comparison, we devised our approach to find all retinal boundaries in our 2 datasets. No feature extraction step was used to improve the experimental results; instead, a single program groupwise curve

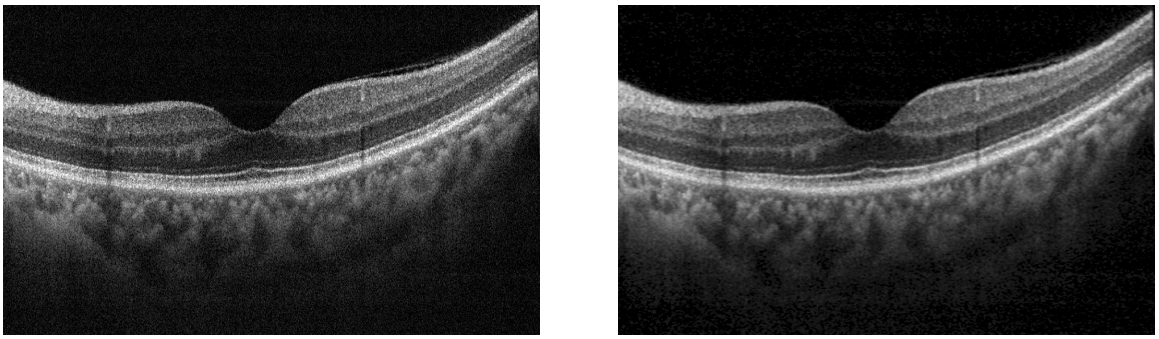

(a) (b)

FIGURE 4. (a) Original OCT image. (b) After intensity normalization.

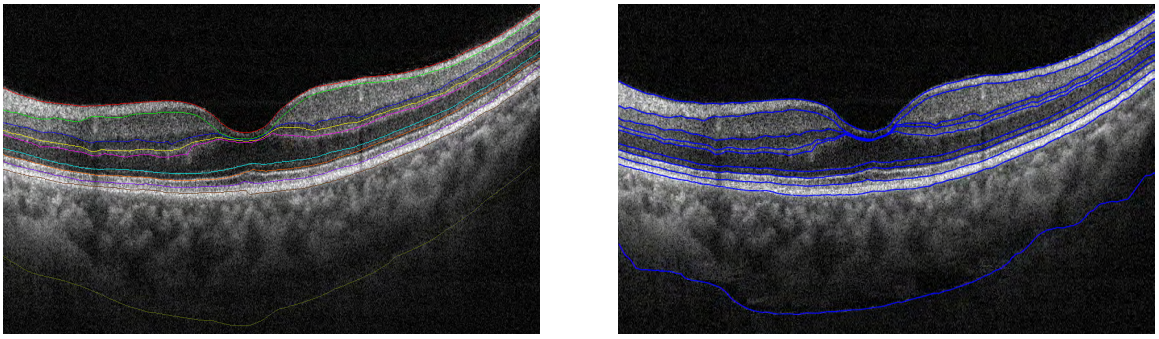

(a) (b)

FIGURE 5. Example slices from the OCT volumes of healthy eyes. (a) manual segmentation results; (b) proposed method.

TABLE 1. Summary of mean unsigned retinal layer positioning errors for dataset1.

	dataset1				
	Obs.1 vs Obs.2	Algo. vs Obs.1	Algo. vs Obs.2	Algo. vs Avg.Obs.	BC vs Avg.Obs.
ILM	1.98 ± 1.06	1.06 ± 0.74	0.78 ± 0.73	0.59 ± 0.47	1.30 ± 1.68
NFL/GCL	2.21 ± 1.14	1.32 ± 1.09	0.68 ± 0.86	1.24 ± 0.96	5.03 ± 4.59
IPL/INL	2.19 ± 0.99	1.42 ± 1.34	0.89 ± 0.98	1.59 ± 1.15	4.49 ± 5.79
INL/OPL	2.08 ± 1.08	1.19 ± 0.91	1.59 ± 1.37	1.14 ± 0.84	5.16 ± 5.84
OPL/ONL	1.81 ± 1.00	1.16 ± 0.88	1.39 ± 1.07	1.10 ± 0.65	4.31 ± 3.13
ONL/OLM	1.88 ± 1.02	1.09 ± 1.73	2.33 ± 1.90	1.49 ± 1.81	3.61 ± 3.32
ISP	1.39 ± 0.90	1.29 ± 0.86	2.24 ± 1.81	0.84 ± 0.75	4.68 ± 5.07
OSP/RPE	1.48 ± 1.02	1.98 ± 1.29	2.33 ± 1.09	2.38 ± 1.23	2.13 ± 2.92
RPE/BRC	1.89 ± 1.22	1.64 ± 1.54	2.56 ± 1.04	2.27 ± 1.27	3.41 ± 3.23
CHR/SCL	2.07 ± 1.14	1.35 ± 1.27	1.17 ± 0.99	2.86 ± 1.87	-
Total	**1.90 ± 1.06**	**1.35 ± 1.17**	**1.56 ± 1.38**	**1.55 ± 1.1**	**3.79 ± 3.95**

Mean ± standard deviation in pixel.

alignment was performed. Fig. 6 illustrates the segmented lesion surfaces on three slices of disease volumes. For our method and the graph-based multi-surface segmentation method, the mean and standard deviation of the unsigned and signed retinal layer positioning errors of all B-scans were computed as listed in Tables 1–4.

D. DISCUSSION

The experimental results show that our framework can accurately segment all the layers—even when their small size and similar textures make the retinal layers difficult to distinguish visually. The proposed method produced segmentations of the retina layers that aligned well with the reference standard, even though the B-scans in dataset1 are cross-sectional slices centered on the fovea. Thus, our approach is robust to fovea, which may have allowed the retinal images containing pathological structures to be segmented by this algorithm. While the conclusion is indirect, the result is promising considering that many retinal pathological structures have a slight similarity to fovea, such as layered structures that are inconspicuous. Simultaneously, the experimental results on dataset2 illustrate that our generative retinal layer seg-

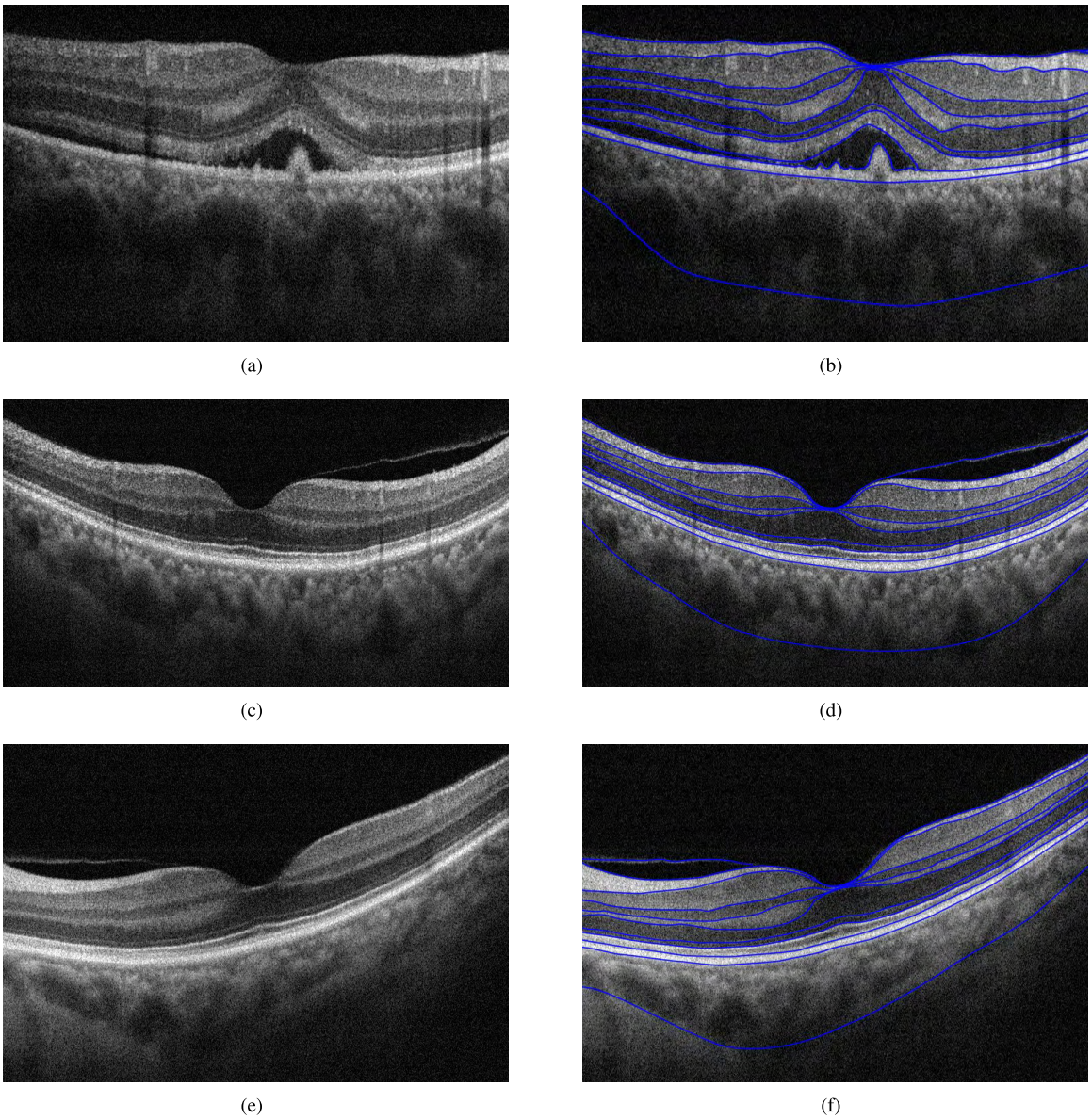

FIGURE 6. Example slices from the OCT volumes of diseased eyes. The left column shows the original OCT cross-sectional scans. The right column shows the segmentation results of all layer interfaces on each cross-sectional of diseased retina by our segmentation method.

TABLE 2. Summary of mean signed retinal layer positioning errors for dataset1.

	dataset1				
	Obs.1 vs Obs.2	Algo. vs Obs.1	Algo. vs Obs.2	Algo. vs Avg.Obs.	BC vs Avg.Obs.
ILM	-1.98 ± 1.06	-1.45 ± 1.07	0.52 ± 0.93	-0.46 ± 0.85	-1.37 ± 1.27
NFL/GCL	-2.18 ± 1.18	-0.40 ± 1.67	1.78 ± 1.52	0.68 ± 1.48	2.80 ± 2.67
IPL/INL	-2.12 ± 1.10	0.57 ± 2.04	2.07 ± 2.05	1.63 ± 1.97	3.04 ± 2.65
INL/OPL	-2.05 ± 1.12	-0.29 ± 1.47	1.75 ± 1.28	0.72 ± 1.26	-4.57 ± 3.7
OPL/ONL	-1.79 ± 1.04	-0.47 ± 1.38	1.32 ± 1.15	0.42 ± 1.16	-3.9 ± 2.60
ONL/OLM	-1.88 ± 1.02	0.49 ± 2.00	2.37 ± 1.98	1.43 ± 1.93	2.26 ± 1.66
ISP	-1.29 ± 1.03	0.73 ± 1.74	2.03 ± 2.05	1.38 ± 1.83	2.34 ± 1.54
OSP/RPE	-1.43 ± 1.08	1.96 ± 1.33	3.40 ± 1.39	2.68 ± 1.25	4.25 ± 7.53
RPE/BRC	-1.68 ± 1.49	1.41 ± 1.75	3.10 ± 2.07	2.5 ± 1.77	-3.94 ± 4.22
CHR/SCL	-2.00 ± 1.25	-1.12 ± 1.48	0.87 ± 1.26	-0.12 ± 1.22	-
Total	**-1.84 ± 1.13**	**0.14 ± 1.59**	**1.92 ± 1.56**	**1.08 ± 1.47**	**0.10 ± 3.09**

Mean ± standard deviation in pixel.

TABLE 3. Summary of mean unsigned retinal layer positioning errors for dataset2.

	dataset2			
	Obs.1 vs Obs.2	Algo. vs Obs.1	Algo. vs Obs.2	Algo. vs Avg.Obs.
1	1.23 ± 1.09	1.19 ± 0.87	1.42 ± 1.02	1.14 ± 0.74
2	1.58 ± 1.36	1.29 ± 1.04	1.16 ± 1.08	1.29 ± 0.88
3	1.25 ± 1.09	1.32 ± 1.02	3.32 ± 2.82	1.32 ± 1.02
4	0.91 ± 0.92	1.25 ± 1.20	1.23 ± 1.17	1.26 ± 1.02
5	1.55 ± 1.14	1.21 ± 0.91	1.19 ± 1.02	1.07 ± 0.91
6	1.27 ± 0.92	1.15 ± 0.77	1.41 ± 1.11	1.14 ± 0.76
7	1.17 ± 1.35	1.02 ± 0.97	1.95 ± 1.22	1.02 ± 0.97
8	1.50 ± 0.84	1.83 ± 0.90	1.07 ± 1.14	1.92 ± 0.81
9	1.92 ± 1.39	1.41 ± 0.76	2.34 ± 1.54	1.40 ± 0.76
10	1.05 ± 1.45	1.29 ± 1.00	1.10 ± 1.22	1.29 ± 1.00
11	7.56 ± 6.65	4.77 ± 2.75	5.32 ± 7.01	2.06 ± 3.74
Total	**1.91 ± 1.56**	**1.61 ± 1.22**	**1.95 ± 1.85**	**1.47 ± 1.15**

Mean ± standard deviation in pixel.

TABLE 4. Summary of mean signed retinal layer positioning errors for dataset2.

	dataset2			
	Obs.1 vs Obs.2	Algo. vs Obs.1	Algo. vs Obs.2	Algo. vs Avg.Obs.
1	-0.76 ± 1.40	-0.33 ± 1.34	0.42 ± 1.70	0.04 ± 1.36
2	0.77 ± 1.94	1.10 ± 1.96	0.33 ± 1.56	0.71 ± 1.48
3	-0.14 ± 1.66	0.96 ± 3.75	1.11 ± 4.22	1.04 ± 3.91
4	-0.58 ± 1.16	-1.23 ± 1.28	-0.65 ± 1.58	-0.94 ± 1.31
5	-1.42 ± 1.29	-1.37 ± 1.21	0.05 ± 1.57	-0.66 ± 1.25
6	-0.95 ± 1.24	0.27 ± 1.53	1.22 ± 1.31	0.75 ± 1.28
7	-1.06 ± 1.13	0.86 ± 1.28	1.68 ± 1.57	1.27 ± 1.32
8	-0.37 ± 1.08	0.29 ± 1.22	1.51 ± 1.84	-0.24± 1.11
9	-0.73 ± 1.28	1.19 ± 1.60	2.26 ± 1.66	1.72 ± 1.54
10	-0.64 ± 1.63	-1.23 ± 1.27	-0.50 ± 1.57	-0.86 ± 1.28
11	-1.56 ± 4.34	-4.57 ± 7.53	-3.92 ± 8.43	-4.25 ± 4.76
Total	**-0.67 ± 1.63**	**-3.98 ± 2.17**	**1.96 ± 2.45**	**-1.09 ± 1.86**

Mean ± standard deviation in pixel.

mentation method based on curve alignment is unique for its accuracy in retinal layer segmentation and its ability to segment any layer without any special modifications.

Tables 1 and 3 provide the results of the means and standard deviations (the shortest distance from a point on an algorithm-produced border to a manually-specified border) of the absolute retinal layer positioning errors between the proposed algorithm and the reference standard. From the results, we can see the following. (1) Most of the deviations are smaller than those computed between the observers. For example, the manual tracings of the two independent observers differed in their segmentations of the total retina by an average of 1.90 pixels, whereas our algorithm differed from the ground truths by an average of 1.55 and 1.43 pixels on two data sets, respectively. (2) The accuracy of the segmentation results on each layer is consistent with the results of artificial segmentation. Experimentally, we calculated that the difference of the two manual segmentation results for the CHR/SCL boundary on dataset2 is 7.56 pixels, which is obviously greater than that of other layers. On the same layer, the difference between the algorithm segmentation result and the reference standard is 2.06 pixels. Similarly, this result is worse than the means from other layers obtained by the proposed algorithm. (3) Our method achieves an average thickness accuracy improvement of approximate 2 pixels compared to the graph-based multi-surface segmentation technique over the layers of the full retina.

Table 2 and Table 4 list the results of the total signed surface positioning errors between the proposed method and the reference standard. The top rows of these tables show the segmentation results of the pathologic region and the remaining rows shows the segmented results of successive retinal layers. As can be seen, the total signed surface positioning errors between the artificial marks were respectively approximately -1.84 and -0.67 pixels. These results indicate that manual segmentation is a subjective process.

V. CONCLUSION AND FUTURE WORK

This paper introduced an early work on semi-automated segmentation of retinal layers from OCT, which can delineate the boundaries of any retinal layer when a single boundary point is manually specified. The powerful segmentation tool integrates segmentation, curve alignment, and joint matching to comprehensively employ the image information derived from each A-scan series. To evaluate the repeatability of the proposed method, we compared the proposed solution with segmentations performed manually by two independent observers. The experimental results demonstrate the proposed method's promising results. The experiment validated that our algorithm is unique for its accuracy in retinal layer segmentation and ability to segment any layer without any special modifications, and that it avoids the drawbacks of the current most-popular method of examining the special characteristics of the retinal layer's area and boundary.

There are several open problems and directions that this work can research deeply in this field. Next, we plan to focus on automatically acquiring the pathological information using the generative model and exploring its roles in auxiliary diagnoses of retinal diseases.

REFERENCES

[1] H. Ishikawa, D. M. Stein, G. Wollstein, S. Beaton, J. G. Fujimoto, and J. S. Schuman, "Macular segmentation with optical coherence tomography," *Invest. Ophthalmol. Vis. Sci.*, vol. 46, no. 6, pp. 2012–2017, 2005.

[2] K. A. Vermeer, J. van der Schoot, H. G. Lemij, and J. F. de Boer, "Automated segmentation by pixel classification of retinal layers in ophthalmic OCT images," *Biomed. Opt. Exp.*, vol. 2, no. 6, pp. 1743–1756, 2011.

[3] D. Koozekanani, K. Boyer, and C. Roberts, "Retinal thickness measurements from optical coherence tomography using a Markov boundary model," *IEEE Trans. Med. Imag.*, vol. 20, no. 9, pp. 900–916, Sep. 2001.

[4] A. Yazdanpanah, G. Hamarneh, B. Smith, and M. Sarunic, "Intra-retinal layer segmentation in optical coherence tomography using an active contour approach," in *Proc. Int. Conf. Med. Image Comput. Comput.-Assist. Intervent.*, 2009, pp. 649–656.

[5] V. Kajić *et al.*, "Robust segmentation of intraretinal layers in the normal human fovea using a novel statistical model based on texture and shape analysis," *Opt. Exp.*, vol. 18, no. 14, pp. 14730–14744, 2010.

[6] Y. Zheng, R. Xiao, Y. Wang, and J. C. Gee, "A generative model for OCT retinal layer segmentation by integrating graph-based multi-surface searching and image registration," in *Proc. Int. Conf. Med. Image Comput. Comput.-Assist. Intervent.*, 2013, pp. 428–435.

[7] A. Lang *et al.*, "Retinal layer segmentation of macular OCT images using boundary classification," *Biomed. Opt. Exp.*, vol. 4, no. 7, pp. 1133–1152, 2013.

[8] Q. Yang *et al.*, "Automated layer segmentation of macular OCT images using dual-scale gradient information," *Opt. Exp.*, vol. 18, no. 20, pp. 21293–21307, 2010.

[9] S. J. Chiu, X. T. Li, P. Nicholas, C. A. Toth, J. A. Izatt, and S. Farsiu, "Automatic segmentation of seven retinal layers in SDOCT images congruent with expert manual segmentation," *Opt. Exp.*, vol. 18, no. 18, pp. 19413–19428, 2010.

[10] S. J. Chiu, M. J. Allingham, P. S. Mettu, S. W. Cousins, J. A. Izatt, and S. Farsiu, "Kernel regression based segmentation of optical coherence tomography images with diabetic macular edema," *Biomed. Opt. Exp.*, vol. 6, no. 4, pp. 1172–1194, 2015.
[11] P. A. Dufour *et al.*, "Graph-based multi-surface segmentation of OCT data using trained hard and soft constraints," *IEEE Trans. Med. Imag.*, vol. 32, no. 3, pp. 531–543, Mar. 2013.
[12] M. K. Garvin, M. D. Abramoff, X. Wu, S. R. Russell, T. L. Burns, and M. Sonka, "Automated 3-D intraretinal layer segmentation of macular spectral-domain optical coherence tomography images," *IEEE Trans. Med. Imag.*, vol. 28, no. 9, pp. 1436–1447, Sep. 2009.
[13] M. K. Garvin, M. D. Abramoff, R. Kardon, S. R. Russell, X. Wu, and M. Sonka, "Intraretinal layer segmentation of macular optical coherence tomography images using optimal 3-D graph search," *IEEE Trans. Med. Imag.*, vol. 27, no. 10, pp. 1495–1505, Oct. 2008.
[14] L. de Sisternes, J. Hu, D. L. Rubin, and M. F. Marmor, "Localization of damage in progressive hydroxychloroquine retinopathy on and off the drug: Inner versus outer retina, parafovea versus peripheral fovea," *Invest. Ophthalmol. Vis. Sci.*, vol. 56, no. 5, pp. 3415–3426, 2015.
[15] H.-J. Lee, M.-S. Kim, Y.-J. Jo, and J.-Y. Kim, "Thickness of the macula, retinal nerve fiber layer, and ganglion cell layer in the epiretinal membrane: The repeatability study of optical coherence tomography," *Invest. Ophthalmol. Vis. Sci.*, vol. 56, no. 8, pp. 4554–4559, 2015.
[16] D. C. Fernández, H. M. Salinas, and C. A. Puliafito, "Automated detection of retinal layer structures on optical coherence tomography images," *Opt. Exp.*, vol. 13, no. 25, pp. 10200–10216, 2005.
[17] S. R. Sadda *et al.*, "Error correction and quantitative subanalysis of optical coherence tomography data using computer-assisted grading," *Invest. Ophthalmol. Vis. Sci.*, vol. 48, no. 2, pp. 839–848, 2007.
[18] Y. Huang *et al.*, "Development of a semi-automatic segmentation method for retinal oct images tested in patients with diabetic macular edema," *PLoS ONE*, vol. 8, no. 12, p. e82922, 2013.
[19] C. Ahlers *et al.*, "Automatic segmentation in three-dimensional analysis of fibrovascular pigmentepithelial detachment using high-definition optical coherence tomography," *Brit. J. Ophthalmol.*, vol. 92, no. 2, pp. 197–203, 2008.
[20] G. J. McLellan and C. A. Rasmussen, "Optical coherence tomography for the evaluation of retinal and optic nerve morphology in animal subjects: Practical considerations," *Veterinary Ophthalmol.*, vol. 15, no. S2, pp. 13–28, 2012.
[21] X. Zhou, M. Zhu, and K. Daniilidis, "Multi-image matching via fast alternating minimization," in *Proc. IEEE Int. Conf. Comput. Vis.*, Dec. 2015, pp. 4032–4040.
[22] Q.-X. Huang and L. Guibas, "Consistent shape maps via semidefinite programming," *Comput. Graph. Forum*, vol. 32, no. 5, pp. 177–186, 2013.
[23] H. Sakoe and S. Chiba, "Dynamic programming algorithm optimization for spoken word recognition," *IEEE Trans. Acoust., Speech, Signal Process.*, vol. ASSP-26, no. 1, pp. 43–49, Feb. 1978.
[24] L. R. Rabiner and B.-H. Juang, *Fundamentals of Speech Recognition*. Englewood Cliffs, NJ, USA: Prentice-Hall, 1993.
[25] F. Zhou and F. De la Torre, "Generalized time warping for multi-modal alignment of human motion," in *Proc. IEEE Conf. Comput. Vis. Pattern Recognit. (CVPR)*, Jun. 2012, pp. 1282–1289.
[26] Y. Chen *et al.* (2015). *The UCR Time Series Classification Archive*. [Online]. Available: www.cs.ucr.edu/~eamonn/time_series_data/
[27] M. G. Baydogan, G. Runger, and E. Tuv, "A bag-of-features framework to classify time series," *IEEE Trans. Pattern Anal. Mach. Intell.*, vol. 35, no. 11, pp. 2796–2802, Nov. 2013.
[28] J. Zhao and L. Itti, "Classifying time series using local descriptors with hybrid sampling," *IEEE Trans. Knowl. Data Eng.*, vol. 28, no. 3, pp. 623–637, Mar. 2016.
[29] E. J. Keogh and M. J. Pazzani, "Derivative dynamic time warping," in *Proc. SIAM Int. Conf. Data Mining*, 2001, pp. 1–11.
[30] Y.-S. Jeong, M. K. Jeong, and O. A. Omitaomu, "Weighted dynamic time warping for time series classification," *Pattern Recognit.*, vol. 44, no. 9, pp. 2231–2240, Sep. 2011.
[31] K. S. Candan, R. Rossini, X. Wang, and M. L. Sapino, "sDTW: Computing DTW distances using locally relevant constraints based on salient feature alignments," *Proc. VLDB Endowment*, vol. 5, no. 11, pp. 1519–1530, 2012.
[32] J. Zhao and L. Itti. (2016). "shapeDTW: Shape dynamic time warping." [Online]. Available: https://arxiv.org/abs/1606.01601
[33] C. Bregler, A. Hertzmann, and H. Biermann, "Recovering non-rigid 3D shape from image streams," in *Proc. IEEE Conf. Comput. Vis. Pattern Recognit.*, vol. 2. Jun. 2000, pp. 690–696.
[34] Y. Dai, H. Li, and M. He, "A simple prior-free method for non-rigid structure-from-motion factorization," *Int. J. Comput. Vis.*, vol. 107, no. 2, pp. 101–122, 2014.
[35] T. S. Cho, S. Avidan, and W. T. Freeman, "A probabilistic image jigsaw puzzle solver," in *Proc. IEEE Conf. Comput. Vis. Pattern Recognit. (CVPR)*, Jun. 2010, pp. 183–190.
[36] Y. Chen and E. Candes. (2016). "The projected power method: An efficient algorithm for joint alignment from pairwise differences." [Online]. Available: https://arxiv.org/abs/1609.05820
[37] D. Pachauri, R. Kondor, and V. Singh, "Solving the multi-way matching problem by permutation synchronization," in *Proc. Adv. Neural Inf. Process. Syst.*, 2013, pp. 1860–1868.
[38] Y. Shen, Q. Huang, N. Srebro, and S. Sanghavi, "Normalized spectral map synchronization," in *Proc. Adv. Neural Inf. Process. Syst.*, 2016, pp. 4925–4933.
[39] J. Yan, M. Cho, H. Zha, X. Yang, and S. Chu, "Multi-graph matching via affinity optimization with graduated consistency regularization," *IEEE Trans. Pattern Anal. Mach. Intell.*, vol. 38, no. 6, pp. 1228–1242, Jun. 2016.
[40] Y. Chen, L. Guibas, and Q. Huang, "Near-optimal joint object matching via convex relaxation," in *Proc. Int. Conf. Mach. Learn.*, 2014, pp. 100–108.
[41] S. J. Russell and P. Norvig, *Artificial Intelligence: A Modern Approach*, vol. 25. Egnlewood Cliffs, NJ, USA: Prentice Hall, 1995, p. 27.
[42] F. Zhou and F. Torre, "Canonical time warping for alignment of human behavior," in *Proc. Adv. Neural Inf. Process. Syst.*, 2009, pp. 2286–2294.
[43] D. P. Bertsekas, *Dynamic Programming and Optimal Control*, vol. 1, no. 2. Belmont, MA, USA: Athena Scientific, 1995.
[44] V. G. Kim, W. Li, N. J. Mitra, S. DiVerdi, and T. A. Funkhouser, "Exploring collections of 3D models using fuzzy correspondences," *ACM Trans. Graph.*, vol. 31, no. 4, p. 54, 2012.
[45] Q.-X. Huang, G.-X. Zhang, L. Gao, S.-M. Hu, A. Butscher, and L. Guibas, "An optimization approach for extracting and encoding consistent maps in a shape collection," *ACM Trans. Graph.*, vol. 31, no. 6, p. 167, 2012.
[46] A. Nguyen, M. Ben-Chen, K. Welnicka, Y. Ye, and L. Guibas, "An optimization approach to improving collections of shape maps," *Comput. Graph. Forum*, vol. 30, no. 5, pp. 1481–1491, 2011.
[47] J. Yan, Y. Li, W. Liu, H. Zha, X. Yang, and S. M. Chu, "Graduated consistency-regularized optimization for multi-graph matching," in *Proc. Eur. Conf. Comput. Vis.*, 2014, pp. 407–422.
[48] S. Boyd, N. Parikh, E. Chu, B. Peleato, and J. Eckstein, "Distributed optimization and statistical learning via the alternating direction method of multipliers," *Found. Trends Mach. Learn.*, vol. 3, no. 1, pp. 1–122, Jan. 2011.
[49] N. Parikh and S. Boyd, "Proximal algorithms," *Found. Trends Optim.*, vol. 1, no. 3, pp. 127–239, Jan. 2014.
[50] J.-F. Cai, E. J. Candès, and Z. Shen, "A singular value thresholding algorithm for matrix completion," *SIAM J. Optim.*, vol. 20, no. 4, pp. 1956–1982, 2010.
[51] R. Cabral, F. De la Torre, J. P. Costeira, and A. Bernardino, "Unifying nuclear norm and bilinear factorization approaches for low-rank matrix decomposition," in *Proc. IEEE Int. Conf. Comput. Vis.*, Dec. 2013, pp. 2488–2495.
[52] M. Baroni, P. Fortunato, and A. La Torre, "Towards quantitative analysis of retinal features in optical coherence tomography," *Med. Eng. Phys.*, vol. 29, no. 4, pp. 432–441, 2007.
[53] A. Bagci, M. Shahidi, R. Ansari, and M. Blair, "Thickness profiles of retinal layers by optical coherence tomography image segmentation," *Amer. J. Ophthalmol.*, vol. 146, no. 5, pp. 679–687, 2008.

WENJUN DUAN is currently pursuing the master's degree with the School of Information Science and Technology, Shandong Normal University of China. Her research interests include medical image processing.

YUANJIE ZHENG was formerly a Senior Research Investigator with the Perelman School of Medicine, University of Pennsylvania. He is currently a Professor with the School of Information Science and Technology, Shandong Normal University, and a Taishan Scholar of the People's Government of Shandong Province of China. He is an acting Vice Dean with the School of Information Science and Technology and the Institute of Biomedical Sciences, Shandong Normal University. His research interests lie in the fields of medical image analysis, translational medicine, computer vision, and computational photography. His ultimate research goal is to enhance patient care by creating algorithms to automatically quantify and generalize the latent information in various medical images for tasks, such as disease analysis and surgical planning through applications of computer vision and machine learning approaches to medical image analysis tasks, and by developing strategies for image-guided surgical intervention.

YANHUI DING is currently an Associate Professor with the School of Information Science and Technology, Shandong Normal University. His research interests include medical image analysis and data analysis.

SUJUAN HOU received the joint Ph.D. degree from Chongqing University and University of Technology, Sydney, in 2015, with the focus on quantum computation and intelligent systems. Her research interests include video data mining, multimedia classification, and pattern recognition.

YUFANG TANG received the Ph.D. degree in signal and information processing from the Beijing University of Posts and Telecommunications. He is currently a Lecturer with the School of Communication, Shandong Normal University. His research interests include pattern recognition, machine learning, data mining, and multimedia signal processing.

YAN XU received the Ph.D. degree in signal and information processing from the Beijing University of Posts and Telecommunications. She is currently a Lecturer with the School of Communication, Shandong Normal University. Her research interests include machine learning, computer vision, and multimedia signal processing.

MAOLING QIN is currently an Associate Professor and a Graduate Student Supervisor with the Department of Information Science and Engineering, Shandong Normal University. She teaches several subjects for bachelor students, including probability and mathematical statistics and digital image analysis and processing, and teaches advanced computer graphics and advanced engineering mathematics courses for graduate students. She works on several projects funded by national and provincial institutions. She has authored or co-authored over 30 academic papers in international conferences and journals. Her research areas include CAGD, CG, and medical image processing.

JIANFENG WU is currently Chief of the Scientific Research Department with the Affiliated Eye Hospital, Shandong University of Traditional Chinese Medicine. He mainly performs clinical, research, and teaching work in ophthalmology and optometry. He has participated in 15 research programs and authored or co-authored 28 research papers. He also serves as a Secretary General of the Ophthalmology Branch, Chinese Association of Integrative Medicine Department Committee. He is a Youth Member of the Chinese Society of Traditional Chinese Medicine Ophthalmology Branch and a Member of the Shandong Province Medical Association Clinical Epidemiology Branch.

DINGGANG SHEN was a tenure-track Assistant Professor with the University of Pennsylvanian. He is currently a Professor of radiology with the Biomedical Research Imaging Center (BRIC), computer science, and biomedical engineering with the University of North Carolina at Chapel Hill. He is currently directing the Center for Image Analysis and Informatics, the Image Display, Enhancement, and Analysis Laboratory, Department of Radiology, and also the medical image analysis core in the BRIC. He was a Faculty Member of the Johns Hopkins University.

HONGSHENG BI is currently the Vice President of the Department of Ophthalmology, branch of the World Federation of Chinese Medicine Societies, the President of the ophthalmology branch, Chinese Association of Integrative Medicine Department Committee, the Deputy Chief of the Cataract Group, National Cataract Academy, a permanent Member of the Ophthalmology Branch, Chinese Medical Association and Chinese Ophthalmologist Association, and the Chairman of the Ophthalmology Branch, Shandong Medical Association and Shandong Ophthalmologist Association. He has involved in clinical, teaching, and research ophthalmology for 33 years and made achievements in cataract, uveitis, and refractive errors. He has undertaken 36 items of the National Natural Science Foundation, the National Key Technology Research, National 973 project, the Science and Technology Plan of Shandong province, and the Natural Science Foundation of Shandong Province. He has authored or co-authored over 300 papers in SCI journals and core journals in China. He was a recipient of first prize of scientific and technological progress in Shandong Province and 28 other science and technology progress awards.